DISTRIBUTION STATEMENT A. Approved for public release; distribution is unlimited.

In-situ and Land-Based Remote Sensing of River Inlets and Their Interaction with Coastal Waters

Eric Terrill, Ph.D.
Director, Coastal Observing Research and Development Center
Marine Physical Laboratory
Scripps Institution of Oceanography
(858) 822-3101, eterrill@ucsd.edu

Award Number: N00014-10-0548

LONG-TERM GOALS

Principal research goals are to characterize the physics which control the river flow across the inlet and the fate of the plume within the coastal ocean. A by-product of the observational program will be the development of sensing capabilities that may have Naval interest.

OBJECTIVES

An observational program applying a broad suite of in-situ and boat-based remote sensing tools to the New River inlet and its interaction with the ocean was implemented during the RIVET I experiment. Of particular interest was the flow of the river through and within the inlet; wave breaking within the inlet as a result of shoaling and wave-current interactions; and the fate, dilution, and transport of the river plume as it discharges into the ocean. The discharge and its subsequent transport was dependent on volume, velocity, momentum and temporal variability of the flow; geometric characteristics of the inlet, channels and receiving waters; extent of a tidal prism within the inlet and influence of tides in modulating the flow; the ocean wave climate and wave current interactions and location of breaking within the inlet; and density differences between the river flow and the synoptic conditions of the coastal ocean into which it discharges. The goal was to develop and implement an observational program to best capture this dynamic and complex environment.

APPROACH

As a result of ONR-sponsorship over the past decade, a significant amount of ocean sensing technologies have been developed or procured by PI Terrill that was utilized for RIVET I. A multi-sensor approach to the science program had the dual benefit of contributing to the development of appropriate river sensing strategies for future Naval applications.

WORK COMPLETED

X-band

Twenty-nine consecutive days (April 25 – May 23, 2012) of X-Band radar data was compiled by the SIO RadarVan. Backscatter was recorded at the highest resolution possible by the WAMOS digitizer:

3m range resolution, and 1/12 degree angular resolution. 1024 range samples were taken each angle, giving a range of over 3km from the RadarVan. 14TB of data was amassed overall. The radar data allows us to analyze the river inlet under the influence of varying river flows, tides, ocean currents, impending waves, and bathymetry.

Figure 1 – SIO X-Band Radar Van deployed at the mouth of the New River

REMUS AUV Surveys

Twenty-six REMUS surveys were performed from May 2, 2012 through May 21, 2012. The primary objectives of the surveys were to map the spatial and temporal evolution of the river discharge into the receiving waters and support the hydrodynamic modeling of the inlet by providing in situ datasets to be used in the calibration of the offshore extents of the modeled velocity field. In addition, we supported the Falk/Guza dye releases with additional in-situ observations outside of the inlet. Additional survey objectives included observations within the inlet, and sidescan sonar imaging of the seafloor. A detailed list of all surveys is provided in Table 1.

Table 1. New River REMUS AUV survey summary.

Survey Date	Mission Type	Location	Tide (UTC)	Start Time (UTC)	End Time (UTC)
5/2/2012	Variability	Inlet Mouth	Low: 14:49	17:48:24	18:15:19
5/2/2012	Variability	Inlet Mouth	Low: 14:49	18:21:46	18:53:41
5/2/2012	Variability	Inlet Mouth	Low: 14:49	18:56:02	19:20:46
5/2/2012	Variability	Inlet Channel	Low: 14:49	19:55:32	20:48:54
5/2/2012	Variability	Inlet Channel	Low: 14:49	19:32:40	19:45:13
5/3/2012	SideScan	Outside Inlet	High: 9:31	11:16:04	13:54:56
5/3/2012	Variability	Inlet Mouth	High: 9:31	14:50:37	15:21:29
5/4/2012	Variability	Outside Inlet	High: 10:25	13:51:27	17:04:17
5/5/2012	MET Survey	Buoy 1 to Buoy 2	High: 11:19	15:32:00	19:48:07
5/6/2012	Dye	Outside Inlet	Low: 18:10	17:12:23	19:33:19
5/6/2012	Dye	Outside Inlet	Low: 18:10	19:43:35	21:03:33
5/7/2012	Dye	Outside Inlet	Low: 19:02	17:13:10	19:04:51
5/7/2012	Dye	Outside Inlet	Low: 19:02	19:22:44	21:46:25
5/8/2012	Dye	Outside Inlet	High: 14:28	17:18:49	19:09:37
5/10/2012	MET Survey	Buoy 1 to Buoy 2	High: 15:53	17:51:58	21:35:05
5/11/2012	Dye	Outside Inlet	Low: 10:54	13:08:43	14:55:48
5/11/2012	Dye	Outside Inlet	Low: 10:54	15:27:24	16:45:35
5/12/2012	Dye	Outside Inlet	Low: 11:52	13:44:50	15:35:26
5/12/2012	Dye	Outside Inlet	Low: 11:52	16:02:37	16:56:28
5/14/2012	River Jet	Outside Inlet	High: 7:21	10:35:27	11:26:52
5/15/2012	River Jet	Outside Inlet	Low: 14:33	18:01:57	19:26:25
5/16/2012	River Jet	Outside Inlet	Low: 15:18	14:36:45	16:27:25
5/17/2012	River Jet	Outside Inlet	Low: 15:58	15:01:27	17:48:13
5/19/2012	Dye	Outside Inlet	Low: 17:13	15:49:44	19:20:35
5/20/2012	Dye	Outside Inlet	Low: 17:49	16:56:53	20:14:00
5/21/2012	SideScan	Outside Inlet	Low: 18:25	19:27:57	21:31:18

Minature Wave Buoys

Buoys were deployed to drift across the shoals during all phases of tidal fluctuations. Figure 2 shows the tracks of all buoy deployments throughout the experiment The focus was to measure the transformation of the wave field as it crossed the tidal shoals and interacted with the inlet currents. Buoys were allowed to both ride in on the flood as well as be pushed out by the ebb tide. The three-directional velocity measurements allowed for wave paramenter observations and drift current measurements.

Figure 2. Buoy tracks for all deployments throughout the RIVET I experiment.

Wind Measurement Buoys

Three metereological buoys (Figure 3) were deployed to measure wind speed and direction as well as longshore wind shear. The closest inshore buoy was moored just offshore of the shoals. Met Buoy 02 was 1km offshore and Met Buoy 03 was 3km off shore to measure the wind speed undisturbed by friction from the land and shoaling waves.

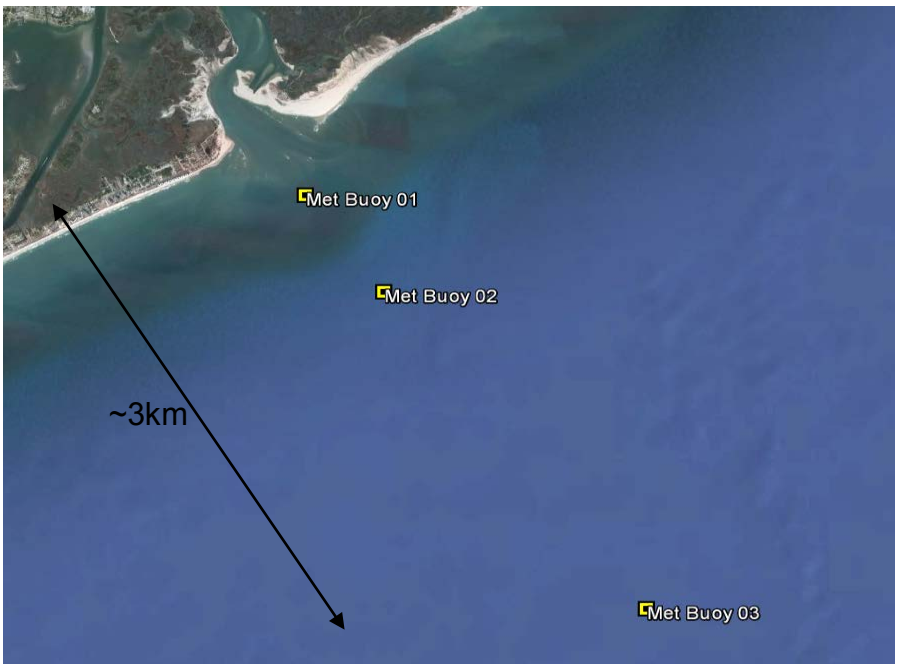

Figure 3. The location of all three metereological buoys deployed off of the New River Inlet.

RESULTS

X-band

Averaging X-Band radar images provides a good indicator of shoaling wave activity in the river mouth. Using the USACE bathymetry, we define an ebb tide shoal line where the water depth decreases below 2m (see Figure 4).

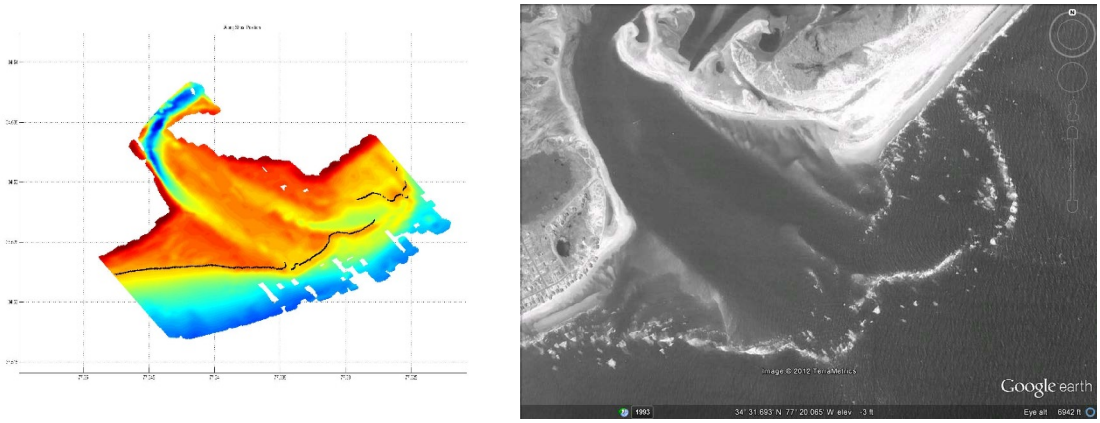

Figure 4. Left - Definition of the ebb tide shoal (black dots) Right – SAR Image showing white water shoaling area (courtesy Hans Graber, RSMAS)

By taking one minute averages and variances of the radar backscatter intensity along the ebb tide shoal definition over a 24 hour period, one can track the tides and water depth, and show where areas of potentially dangerous shoaling are occurring. Figure 5 shows the backscatter average data along the ebb tide shoal line, and the corresponding water depth from an in-situ pressure sensor deployed by WHOI.

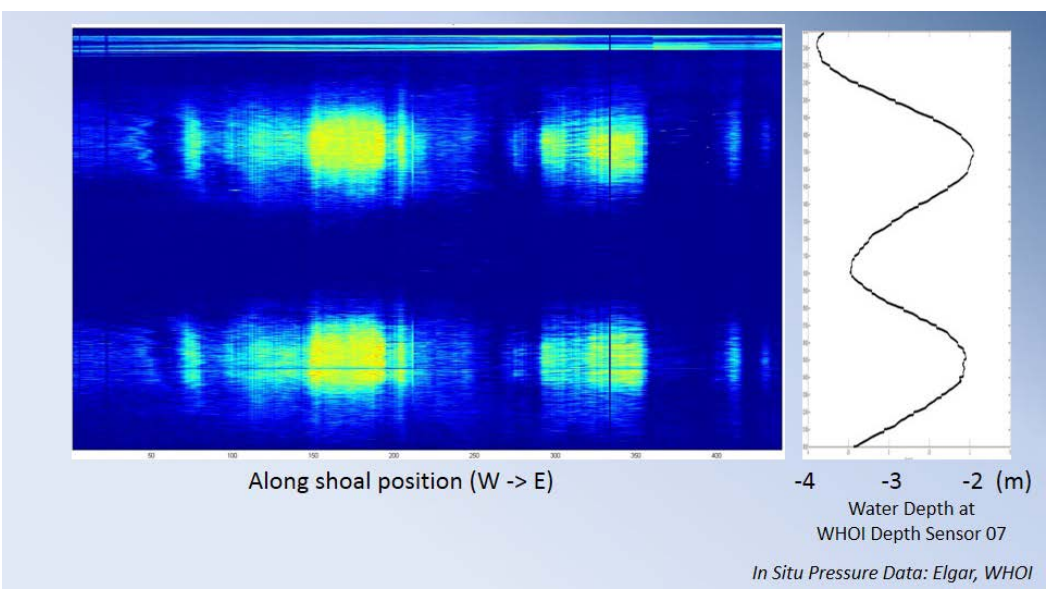

Figure 5. Backscatter average along ebb tide shoal line, showing varying shoaling activity, and observed water depth

Incident ocean wave analysis can be performed using the X-Band radar images. On May 19 at 16:30 UTC, the offshore CDIP buoy 190 was reporting the impending waves having a 1 meter significant wave height, 7.7s peak period, from 129 degrees. Using the X-Band backscatter from the New River channel marker buoy, and the SIO developed 3D wave inversion software, we can see the impending wave spectrum change as the ocean waves approach the river inlet. Figure 6 shows the wavenumber-frequency spectrum for that same time period.

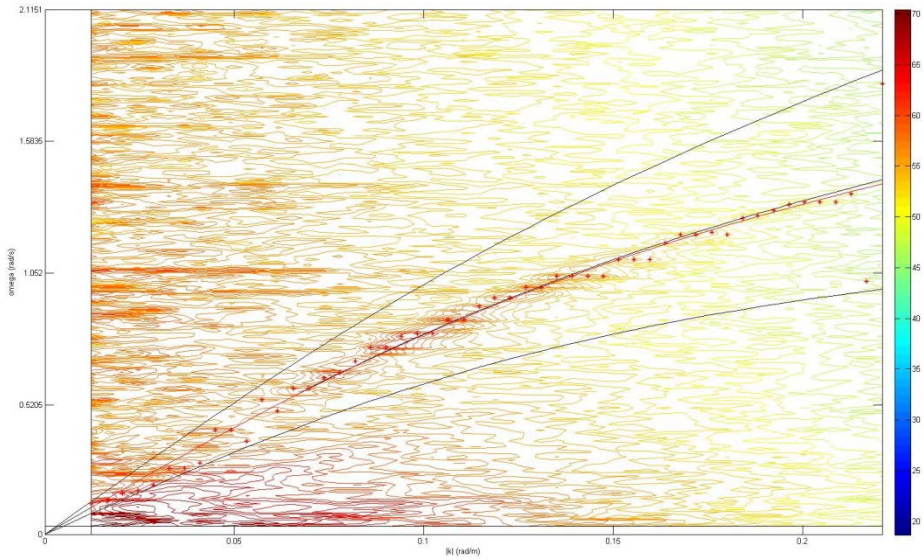

Figure 6. Wavenumber vs. frequency spectrum at the New River channel marker on May 19, 2012 at 16:30 UTC

In Figure 6, the red asterisks mark the peak of the spectral energy along a shifted dispersion relationship curve. In deep water, the waves reported by CDIP buoy 190 would have a wavenumber of 0.068 rad/m, a wavelength of 92m, and a celerity of 12 m/s. In this case the impending waves are shifted down in frequency by the outgoing tide and river plume, in addition the waves are shifted up in wavenumber due to the 8 meter water depth at the channel marker. The shifted dispersion relationship (middle black line) is then "flattened" out compared to the same waves in deep water.

Taking this analysis a step further, we can perform the same spectral analysis closer to shore over the shoals (Figure 9). Now the spectrum is even more linearized towards a very shallow dispersion relationship with tide and river plume (current) effects ($\omega = kh + \mathbf{k} \cdot \mathbf{U}$). An ongoing area of our research is to develop a non-linear inversion method to extract current and depth from these 3D X-Band image inversions. Preliminary efforts have shown some success, but the method still needs refining.

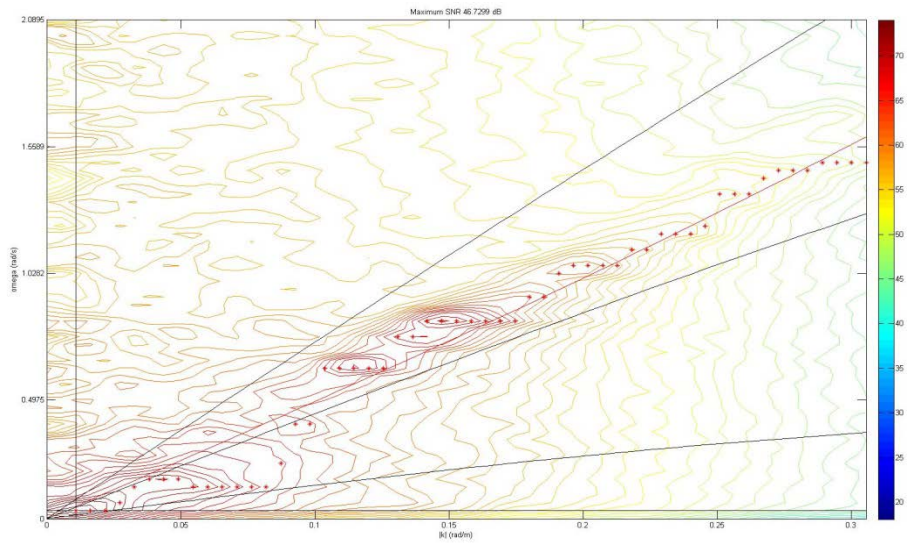

Figure 9. Wavenumber vs. frequency spectrum over the shoals at the mouth of the New River Inlet for May 19, 2012 at 16:30 UTC.

By completing the wave inversion, and plotting the resulting wave field over the shoal, we can produce Figure 10. This clearly shows the waves interacting with the shoals, as well as the old and new channels. The new channel has waves breaking across it at the ebb tide shoal line (previously defined).

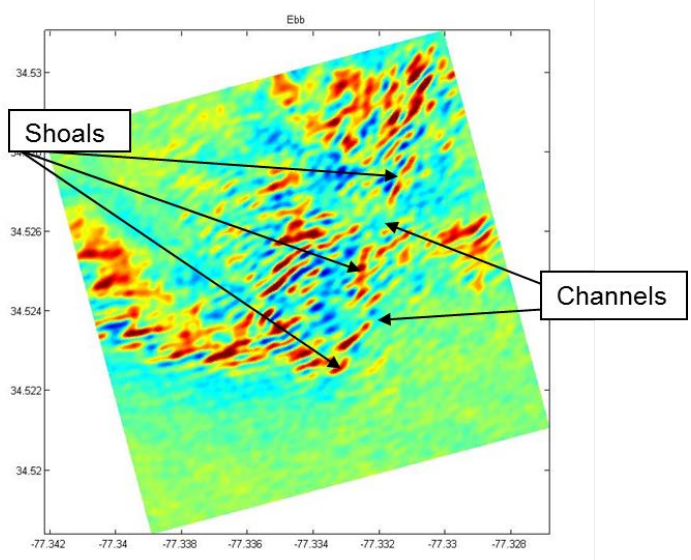

Figure 10. X-Band radar wave inversion results

In Figure 10, one cans see the impending waves shorten up in wavelength, progress throught the channels, refract towards (and break on) the shallow shoals. Previous research in current and bathymetry measurement using airborne imagery (Dugan, Pietrowski), X-Band radar (Bell), PIV analysis (Ahmed, Takewaka), and tomography (Plant, Holland, Haller) has proven effective in a linear shoreline environment. The complex bathymetry of the New River Inlet challenges those methods.

Using concepts inherent in the literature, we can decompose the measured wavenumber frequency spectrum, and extract (filter) out a single frequency component, which has many wavenumber components contributing to it due to the bathymetry. By inverting this single frequency component back into the time domain, we can see how the bathymetry and current effect those singular waves. A simple ray tracing technique can be applied to the resulting images as shown in Figure 11.

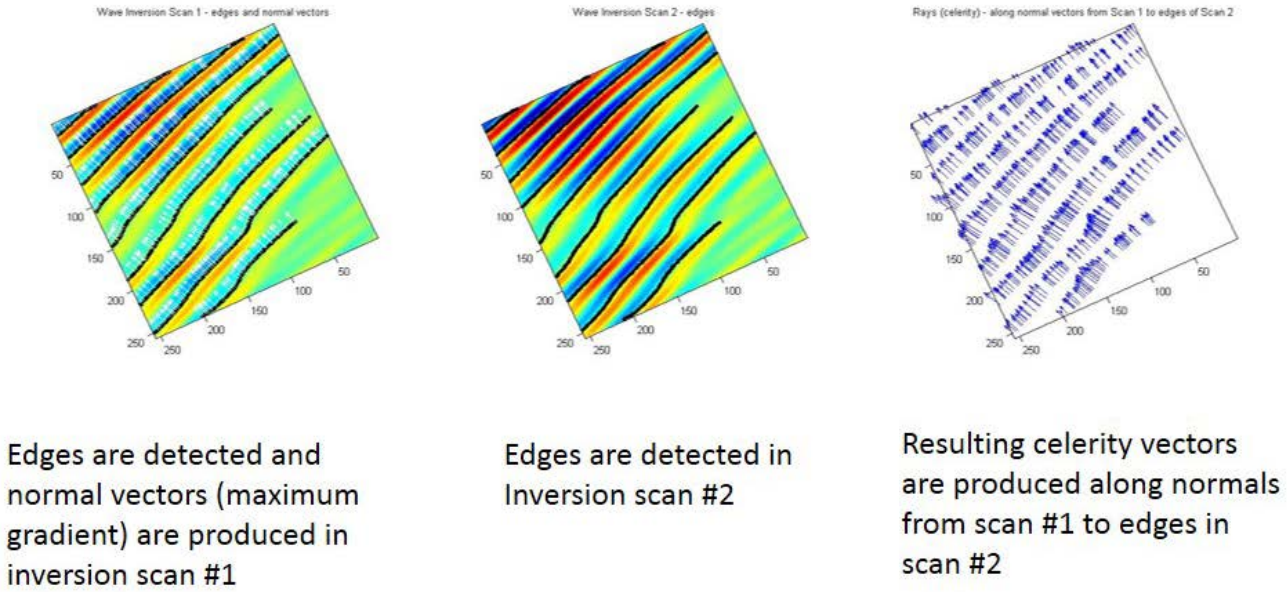

Figure 11. Ray tracing algorithm to determine wave celerity and bathymetry

The resulting celerity is then plotted in color over the USACE bathymetry in Figure 12. While not perfect, this simple method shows some promise to determine complex bathymetry with tidal and river current effects. Darker orange indicates higher celerity, yellow indicates lower celerity. One can see the waves slow down as they approach the shoal. Deeper channels and shallow mounds are also indicated in the celerity field. This is an ongoing area of our research.

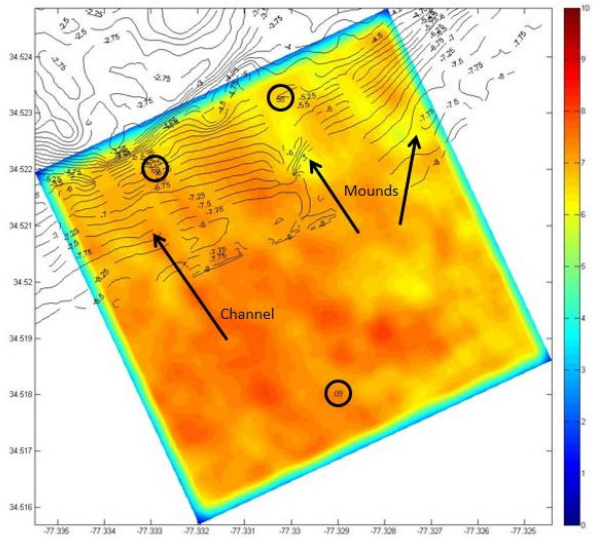

Figure 12. Celerity map and associated bathymetry

New River Morphology Analysis

The X-band radar signal of the New River Inlet is also being analzyed to determine the temporal variability of seabed morphology over the month long May 2012 experiment. More specifically, the radar backscatter intensity during low tide is being utilized to determine the movement of prominent features such as inlet navigation channels and shoaling regions. These prominent features are illustated in the bathymetry map of the Inlet (Figure 14a). An overlay of the radar backscatter intensity onto the bathymetry map (Figure 14b) displays the correlation between shallow shoals and increased radar intensity. During low tide the images delineate the borders of the New River channels and shallow regions.

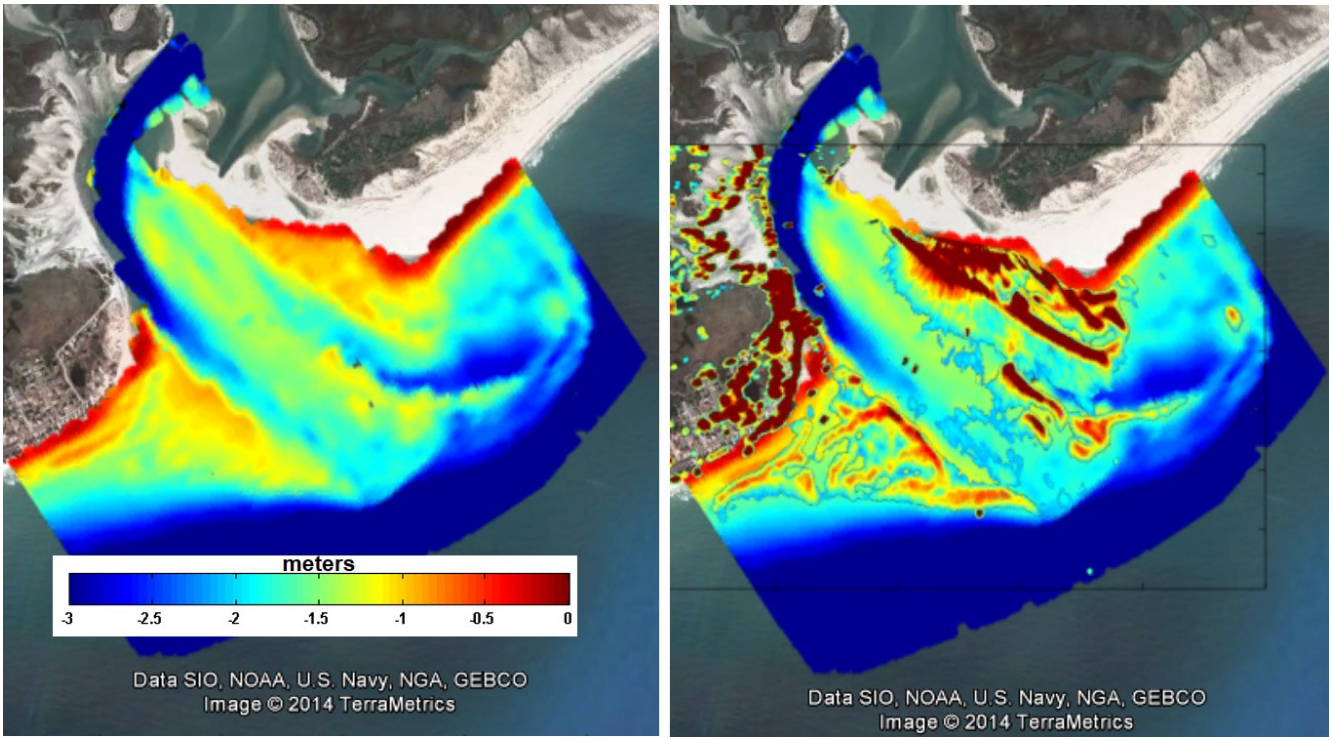

Figure 14. Overlay of X-band radar intensity imagery on bathymetry (in meters) observed by the US Army Corps of Engineers Field Research Facility on 5/2/2012. The radar intensity delineates the spatial boundaries of the inlet including shallow shoaling regions.

A pressure sensor located within the main channel was used to synchronize the time period in which to average radar intensity on different days. Backscatter intensity was averaged hourly at a median depth of 2 m (i.e., data range froms 0.5 hrs before 2 ft depth and 0.5 hrs after 2 ft depth). The averages yield high resolution images that delineate areas of high radar returns due to surface disturbances generally caused by shoaling and wave breaking (Figure 15). A change in the position of areas of high radar intensity suggests a change in the underlying bathymetry (Figure 15a and15b). The 5/2/2012 high gradient boundary (white dotted line) along the main channel shifts in a southwesterly direction during the course of the May 2012 experiment as observed by the 5/10/2012 and 5/17/2012 radar intensity imagery (Figure 15b and Figure 16b). Bathymetry observations from 5/2/2012 and 5/17/2012 are used to determine the feasibility of using radar intensity imagery to assess the temporal variability of shoals within the New River Inlet.

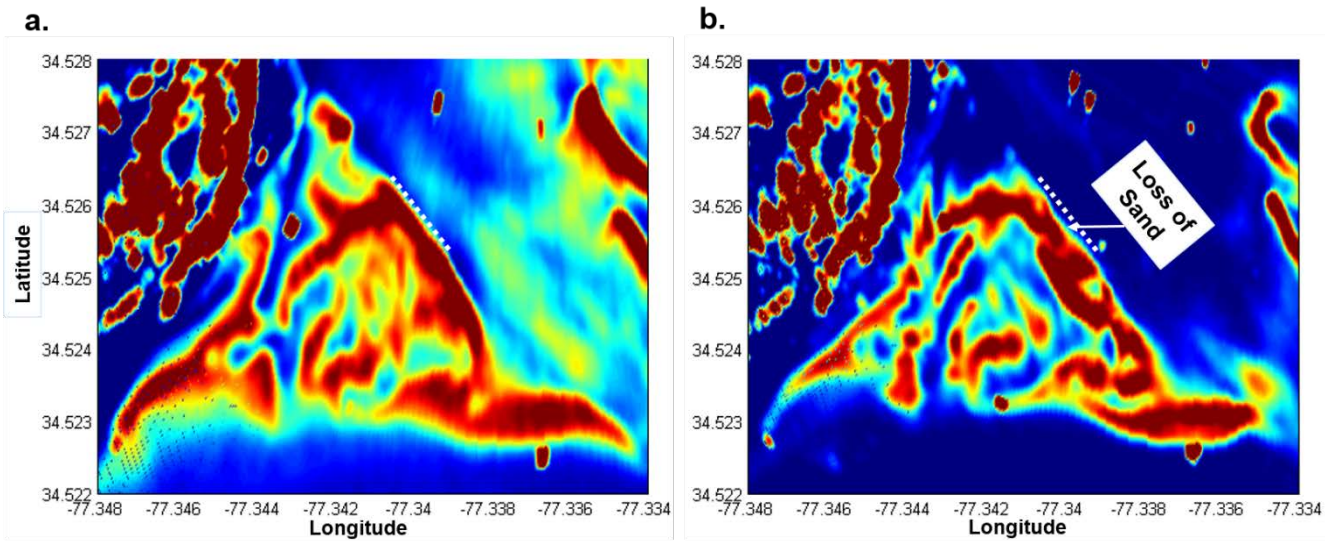

Figure 15. Comparison plot of 1-hour averaged radar imagery for (a) 5/2/2012 and (b) 5/10/2012. The white dotted line defines a high gradient signal boundary along the main channel on 5/2/2012.

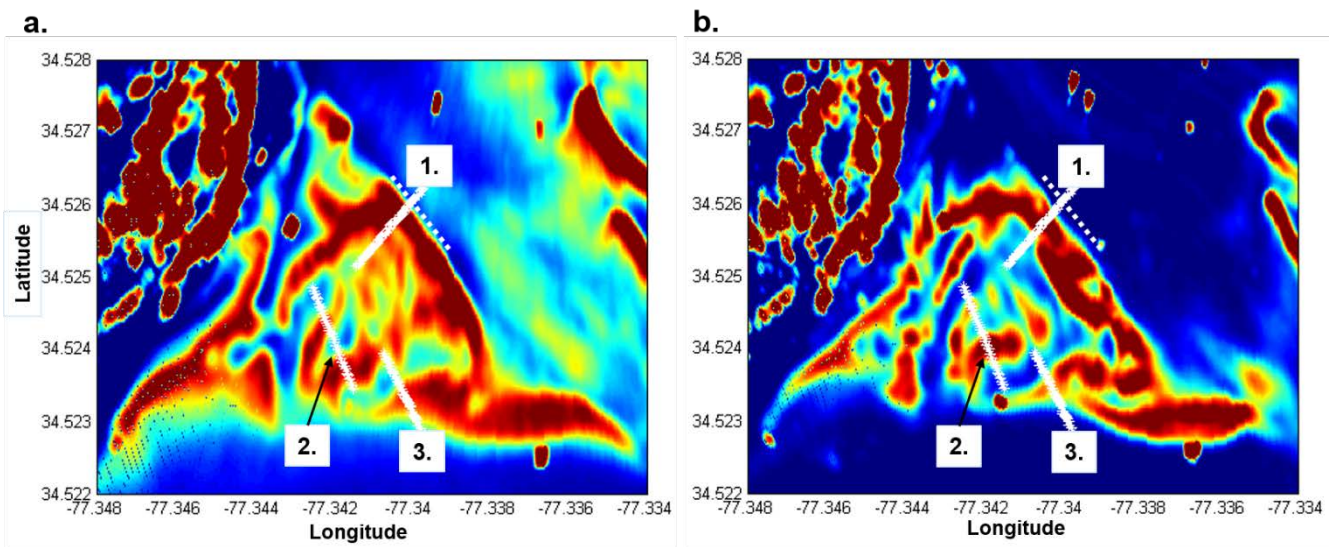

Figure 16. Comparison plot of 1-hour averaged radar imagery for (a) 5/2/2012 and (b) 5/17/2012. The numbers mark linear transects chosen to illustrate the temporal variability of the underlying shoal locations from 5/2/2012 to 5/17/2012.

Three transects were chosen to determine the morphological movements of the shoals and the response of the radar signal to the variability of their locations. Transect 1 was utilized to assess the mechanism responsible for the change in position of the high gradient boundary from 5/2/2012 to 5/17/2012 (Figure 16). A cross-section of the bathymetry along this transect for each observation date shows a significant amount of sand loss from 5/2/2012 to 5/17/2012 (Figure 17a). The loss of sand results in a decrease in the slope along the main channel which shifts the radar intensity signal in a southwesterly direction (Figure 17b).

Analysis of the underlying shoals of transect 2 and 3 suggest the radar intensity signal can be used to estimate the movement of the shoals. For each transect, the peak radar signal generally corresponds with a minimum depth of the bathymetry cross-section (Figures 18 and 19). The bathymetry data along transect 2 shows a ~15 m (from 25 m to 40 m) shift of the shoal in a northwestern direction (Figure 18a). The second shoal along transect 2 shows a similar shift of ~15 m in the same direction. The cross-section of the radar intensity along the same transect shows the same pattern of movement (Figure 18b).

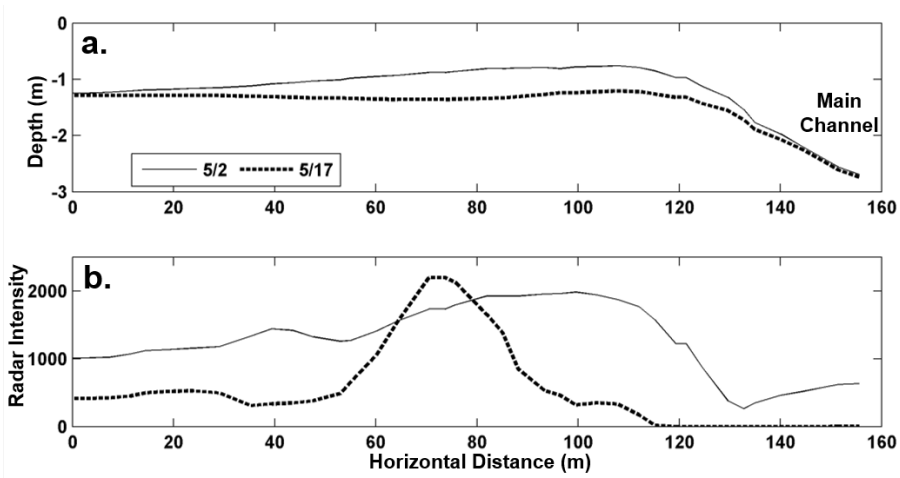

Figure 17. (a) Bathymetry cross section comparison between 5/2/2012 and 5/17/2012 along sampling transect 1 denoted in Figure 16. (b) Radar intensity comparison between 5/2/2012 and 5/17/2012 along transect 1. The origin of the x-axis corresponds with the western most point of the transect.

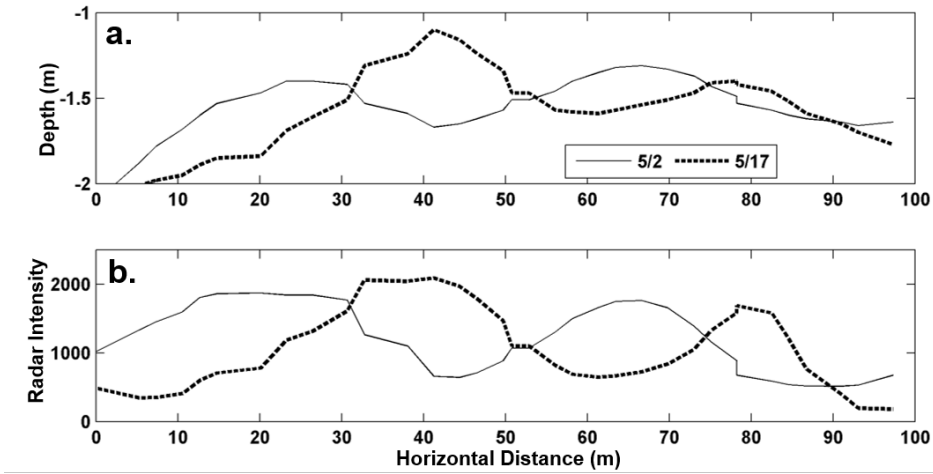

Figure 18. (a) Bathymetry cross section comparison between 5/2/2012 and 5/17/2012 along sampling transect 2 denoted in Figure 16. (b) Radar intensity comparison between 5/2/2012 and 5/17/2012 along transect 2. The origin of the x-axis corresponds with the southernmost point of the transect.

The cross-sections of bathymetry and radar intensity along transect 3 show a similar pattern to that observed along transect 2. The peak in radar intensity signal approximately correlates with the minimum depths along the transect. Both the bathymetry and the radar signal show a movement of ~ 10 m of the shoal along the transect (northwest direction).

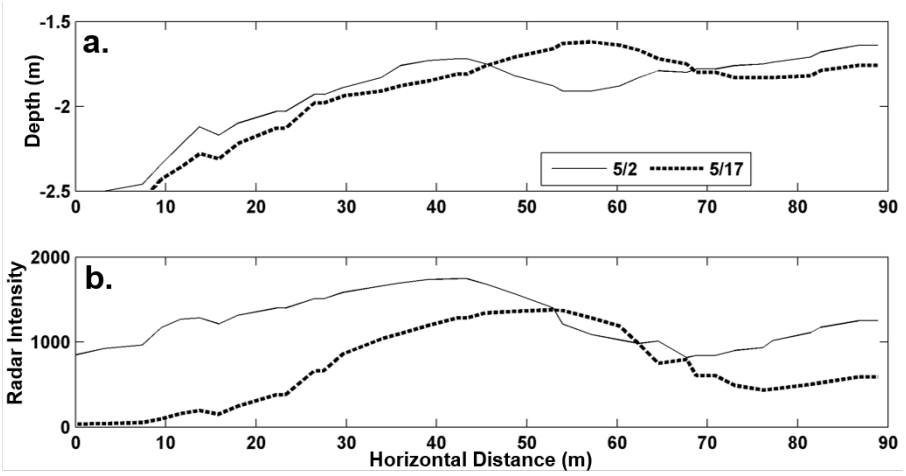

Figure 19. (a) Bathymetry cross section comparison between 5/2/2012 and 5/17/2012 along sampling transect 3 denoted in Figure 16. (b) Radar intensity comparison between 5/2/2012 and 5/17/2012 along transect 3. The origin of the x-axis corresponds with the southern most point of the transect.

Comparisons of bathymetry data and radar intensity signals shows a correlation between areas of minimum depths (shoals) and peaks in radar intensity. This relationship suggests that the radar signal can be used to assess the temporal variability of inlet shoals in the absence of bathymetry data.

REMUS AUV Surveys

The AUV was utilized to target the dynamic transitional region between the near and far-fields of the New River Inlet jet discharge during maximum ebb tide. A brief summary of results are presented below.

We estimated a depth-averaged velocity field computed from DVL observations for the 5/17/2012, 5/19/2012, and 5/20/2012 surveys using a sophisticated statistical method (2D divergence-free (DF) spatial interpolator). We compute the averaged depth from 1 m (relative to the water surface) to the maximum observed depth of the plume in each survey. The resulting velocity field was used to compute the composite Froude numbers of the near- to far-field transitional region (Figure 20). The resulting maps are not synoptic due to the length of the survey (~ 2.5 hrs), and instead should be viewed as a near-synoptic depiction of the evolution of the discharge plume as it advects offshore. The transition from the near- to far-field of a river plume is defined by the change of flow from supercritical to subcritical which is evident in each survey. The 5/17/2012 survey (Figure 20a) was performed under ideal deployment conditions (i.e. minimal winds and waves) which yielded a transition from supercritical to subcritical flow that occurs at approximately transect 3 ($Fr < 1$). A minimal area of Froude numbers greater than 1 was observed along transect 3 suggesting that this marks the offshore extent of the near-field plume.

The 5/19/2012 survey was performed under significantly different oceanic conditions due to a sustained northeasterly wind of ~ 7 m/s resulting in a sea state with significant wave heights of approximately 1.5 – 2 m. The composite Froude numbers from this survey suggest the alongshore wind-driven currents influenced the plume characteristics by narrowing its alongshore spatial extent (after transect 3) as the plume moves offshore when compared to the 5/17/2012 survey (Figure 20a). The greatest amount of alongshore dispersion occurred after transect 3 during the 5/17/2012 survey (minimal wind). In the near-field, differences in the cross-shore extents are also evident between the 5/17/2012 survey (~ 700 m from origin) and the 5/19/2012 and 5/20/2012 surveys (~ 1000 m from origin).

The influence of wind forcing on the plume transport is visible in the CDOM signatures of the plumes and the contrast of the plume dispersal between the 5/17/2012, 5/19/2012, and 5/20/2012 surveys. Figure 21 shows the progression of the plumes from near-shore to offshore and their associated characteristics that are a result of the ambient environmental conditions. The CDOM maps, a scalar indicative of the plume concentration, suggest that the cores of the 5/17/2012 and 5/20/2012 plumes remain coherent to a shore normal distance of approximately 1280 m and 1480 m (transect 6), respectively (Figure 21a and 21c). In contrast, the 5/19/2012 CDOM maps show that the plume undergoes significant mixing due to the momentum of the plume interacting with the coastal mixing processes set up by a strong northeasterly wind. We observed that the influence of the background mixing processes on the stratification of the receiving waters influence the depth of the plume. In the far-field, the cores of the 5/19/2012 and 5/20/2012 plumes are approximately two times the depth of the 5/17/2012 plume depth (~4 m compared to ~2 m). The stratification for each survey and its effect on plume depth is illustrated in Figure 9. We found that the ambient salinity during the 5/17/2012 survey (Figure 22a) was denser than that observed during the 5/19/2012 and 5/20/2012 surveys (Figures 22b and 22c), which is one of the factors contributing to the observed differences in plume depths.

Mixing within the near- to far-field transitional region was further analyzed using the depth-averaged velocity fields estimated by the DF method. The fixed ADCPs recorded minimal variability in current direction and magnitude during the first three transects (~ 1 hr) of each survey allowing for a near-synoptic estimate of the velocity field. The interaction of the discharge plume with localized oceanic conditions for each survey resulted in the three distinct flow fields. The minimal sea state during the 5/17/2012 survey yielded a southeastward plume direction driven by a low variability current field. In contrast, a persistent northeasterly wind during the 5/19/2012 survey advected the lower momentum old channel plume parallel to the wind direction after transect 2 (Figure 23a). As a result, an eddy is setup adjacent to the main plume that entrains the old channel plume water as observed by its shoreward advection before momentum from the main channel discharge forces the old channel plume offshore causing a convergence of the two water masses.

The influence of the variable current field on the salinity field is evident in Figure 22b. A separate salinity signature than that from the main channel discharge is evident northeast of the main plume discharge (right side of contour panels in transect 1 and 2) suggesting two distinct water masses. By viewing the salinity map in conjunction with an estimated map of the velocity field (Figure 23a), we can determine the mechanism driving the variable salinity observed in transects 1 and 2. The reference numbers 1 – 4 in transect 2 of Figures 22b and 23a spatially correlate the two figures allowing for direct comparison of salinity and current observations. The development of an eddy is observed between the old and new channels which advects offshore (between transects 2 and 3) from the old channel discharge waters shoreward (point 4) where the water mass circles the eddy origin at point 3

(which exhibits slightly lower salinity values) and discharges back offshore at point 2. The gradient between the main channel observed salinity (point 1) and point 2 suggest the two water masses do not converge until advected beyond transect 2.

The merging of the two plumes and the conditions created by the surface wave field during the 5/19/2012 survey produced a complex and dynamic mixing region. Critical *Ri* numbers throughout the region (inside and outside of the plume) suggest the current velocity shear in the region was dominant over the vertical stratification, creating an unstable region and increasing the potential for mixing. The influence of this unstable region on the CDOM and salinity signatures of the plume is evident in Figures 21b and 22b with higher observed mixing rates than that observed during the 5/17/2012 survey (Figure 21a and 22a).

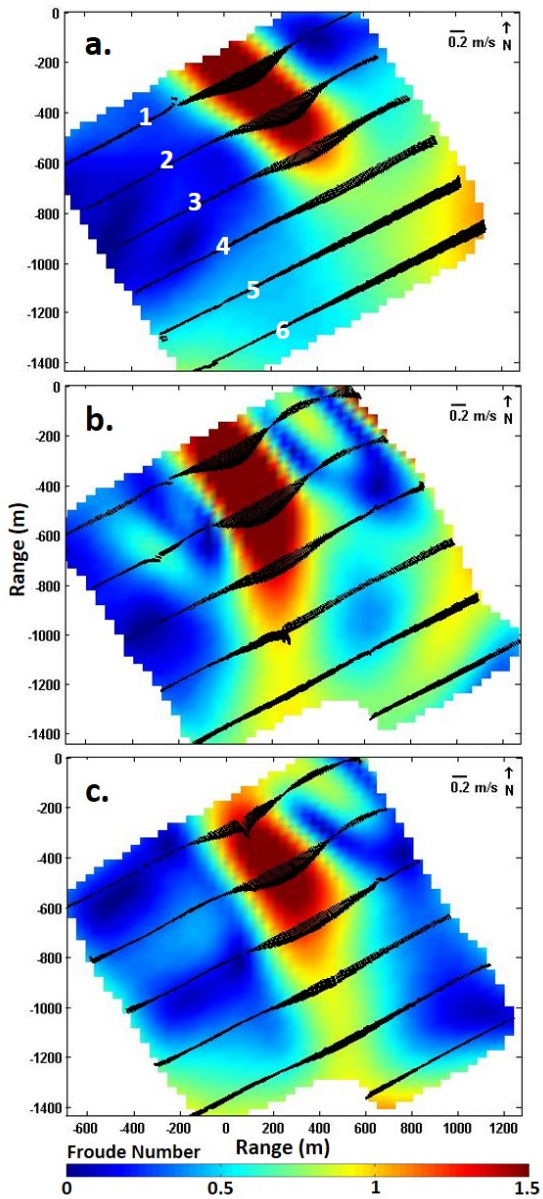

Figure 20. Estimated composite Froude number fields for the (a) 5/17/2012, (b) 5/19/2012, and (c) 5/20/2012 surveys based on AUV velocity measurements (black arrows). Each transect in (a) is labeled with a transect number (1 thru 6). We restrict the velocity estimates to those with ratios of error to signal variance smaller than 0.3. The approximate discharge origin is located at (0,0).

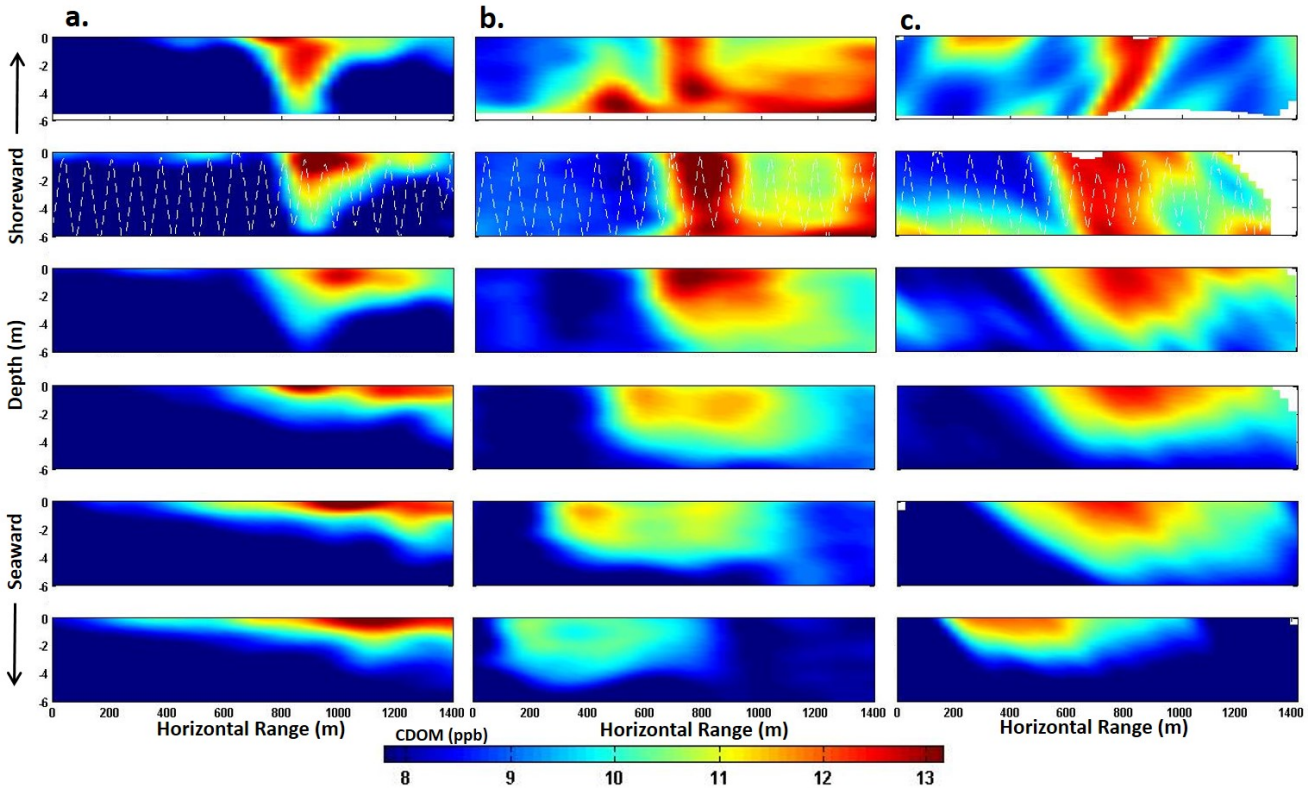

Figure 21. CDOM plots of successive transects that followed the discharge plume offshore for the (a) 5/17/2012, (b) 5/19/2012, and (c) 5/20/2012 surveys with transect spacing of ~200 m, 240 m, and ~240 m respectively. The resolution of the observed data is shown by the AUV path in transect 2 for each date (dotted lines). Blank regions without coloring indicate regions with insufficient data.

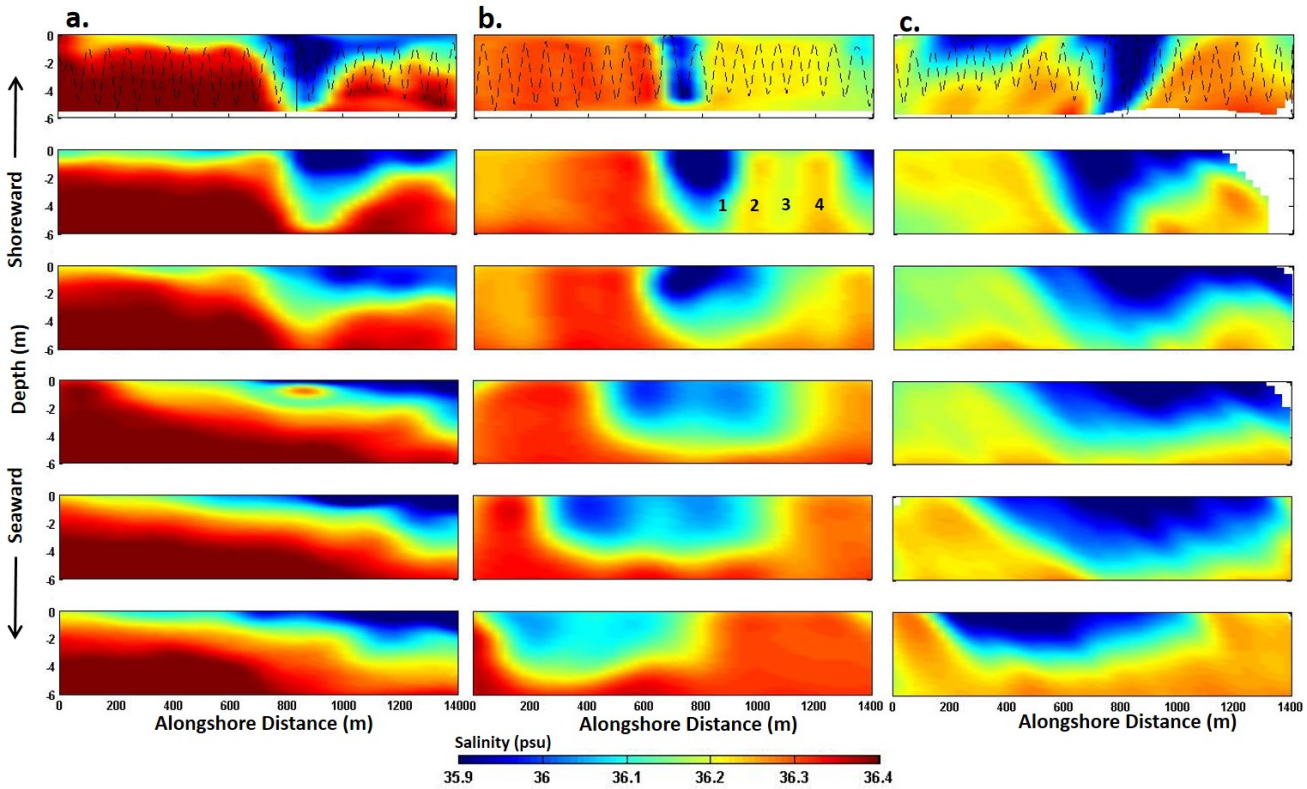

Figure 22. Salinity plots of successive transects that followed the discharge plume offshore for the (a) 5/17/2012, (b) 5/19/2012, and (c) 5/20/2012 surveys. The AUV path (observed data resolution) is shown in the first transect (top figure) for each survey. The numbers shown in transect 2 (5/19/2012) denote separate water masses that result from an eddy located at number 3.

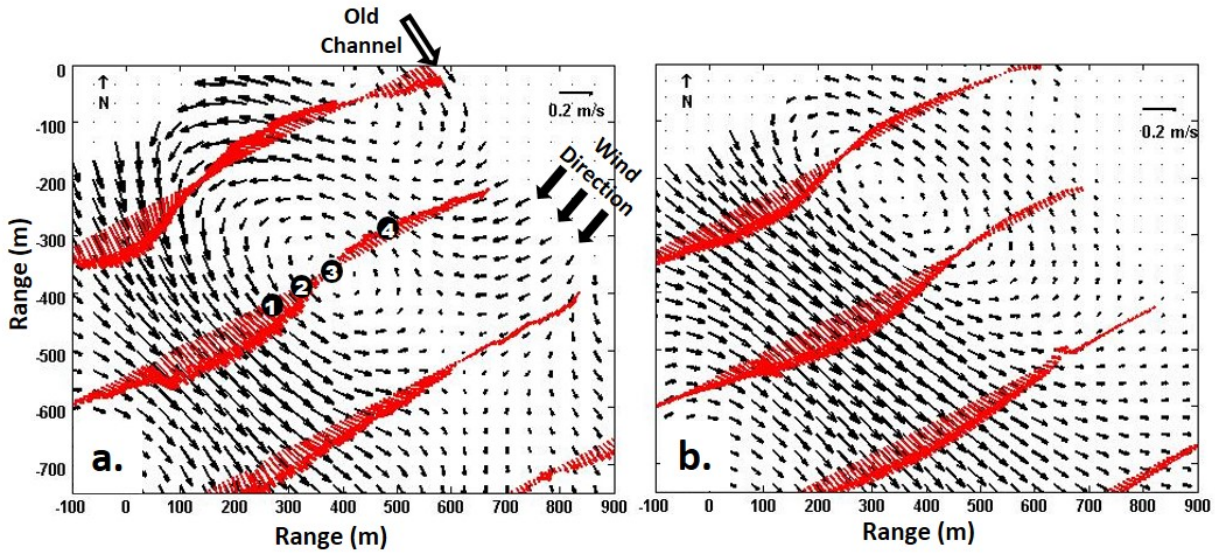

Figure 23. Depth-averaged current field (1 – 5 m) generated from observed DVL velocity data (red arrows) for the (a) 5/19/2012 and (b) 5/20/2012 surveys using the DF method. For reference we include number labels on transect 2 (5/19/2012) that are spatially consistent with the numbers in Figure 9b.

A comparative analysis was performed between AUV observed velocities and modeled velocity fields provided by the Ocean Engineering Laboratory at the University of Delaware. A nearshore community model, NearCoM-TVD, was utilized to simulate hydrodynamics under the interaction of tides and waves at New River Inlet. NearCoM-TVD couples the spectrum wave model Simulating Waves Nearshore (SWAN) [*Booij et al.,* 1999] and a two-dimensional horizontal (2DH) nearshore circulation model SHORECIRC [*Svendsen et al.,* 1984; *Shi et al*., 2003], which incorporates the mixing effect induced by waves. For tidal inlet applications, we verify the NearCoM-TVD is appropriate using the semi-analytical solution of *Keulegan* [1967] for the maximum ebb velocity through the channel [*Chen et al*., 2014].

Observed depth-averaged velocities from the 5/17/2012 and 5/19/2012 AUV surveys were utilized to determine the dominant hydrodynamic mechanisms for the New River Inlet NearCoM-TVD. The preliminary modeled results show that, during ebb tide, the simulated main discharge reaches a maximum velocity of ~1.0 m/s in the inlet channel and then decreases to ~ 0.3 m/s at transect 1. Initial comparisons between model results and observed AUV depth-averaged velocities show a spatial difference in the location of the discharge jet as it advects offshore especially in 05/19/2012 survey (Figure 24). The spatial disparity between the initial model results and observed AUV data is caused by the inability of the model to adequately capture all the processes in typical coastal modeling systems. For the New River Inlet simulations, the bottom friction was a dominant process effecting the spatial accuracy of the discharge. We parameterize the bottom friction in the preliminary model results (Figure 24) using discharge velocities and a drag coefficient caused by the current. However, bottom friction values are dependent on several dynamic variables (e.g., discharge velocity, grain-related roughness, and apparent roughness caused by waves) which can alter the discharge response. When we vary the bed roughness lengths (z_o) the model simulations suggest that the direction of the main discharge is not sensitive to a given median grain size. Conversely, the nonlinear wave-current interaction enhances bottom friction, making its inclusion in the parameterization of the bottom boundary layer (BBL) essential [*Soulsby et al.,* 1997]. Waves in shallow water regions are dominated by their interaction with the bottom which is dependent on several variables including wind speed (i.e., wave height), wave propagation, non-linear interactions, and energy decay [*Padilla-Hernandez and Monbaliu*, 2001]. The availability of high resolution velocity observations of the receiving waters that we compare with the model simulations, were key to determining the appropriate parameterization of bottom friction used in the numerical model. The increased accuracy of the spatial location of the main discharge is evident when the wave-current interaction in the bottom boundary layer is considered (Figure 25).

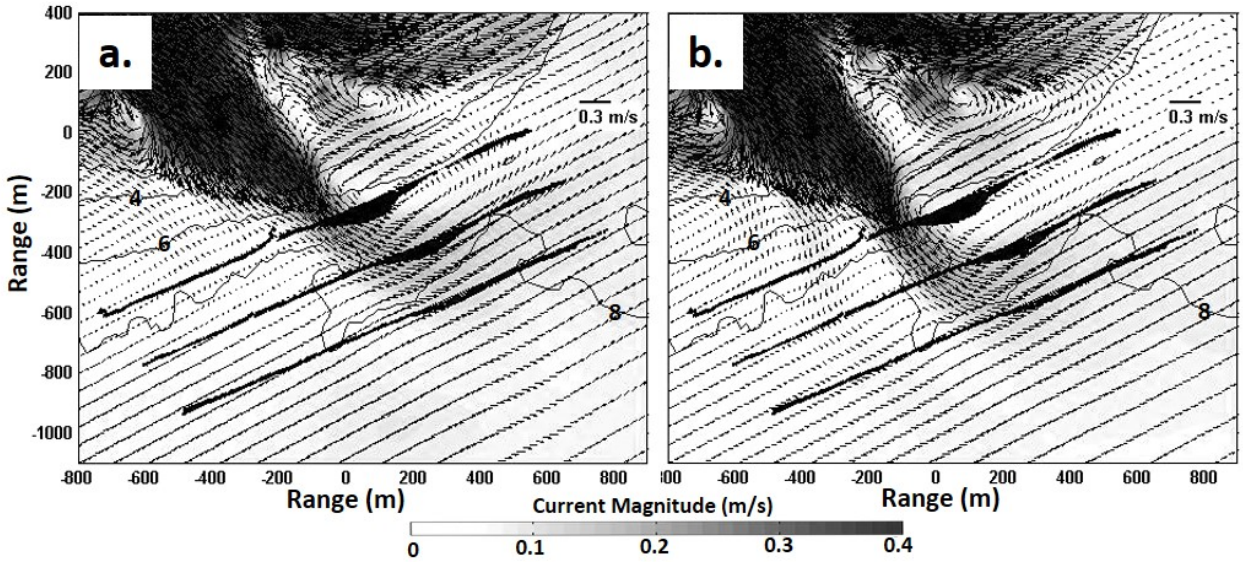

Figure 24. Depth-averaged velocity model output (black arrows, high resolution grid) overlaid with depth-averaged AUV velocity outputs for transects 1 through 3 (dark black arrow) for the (a) 5/17/2012 and (b) 5/19/2012 surveys. Bottom friction for current flow only is assumed for model runs. Numbers denote contours in meters.

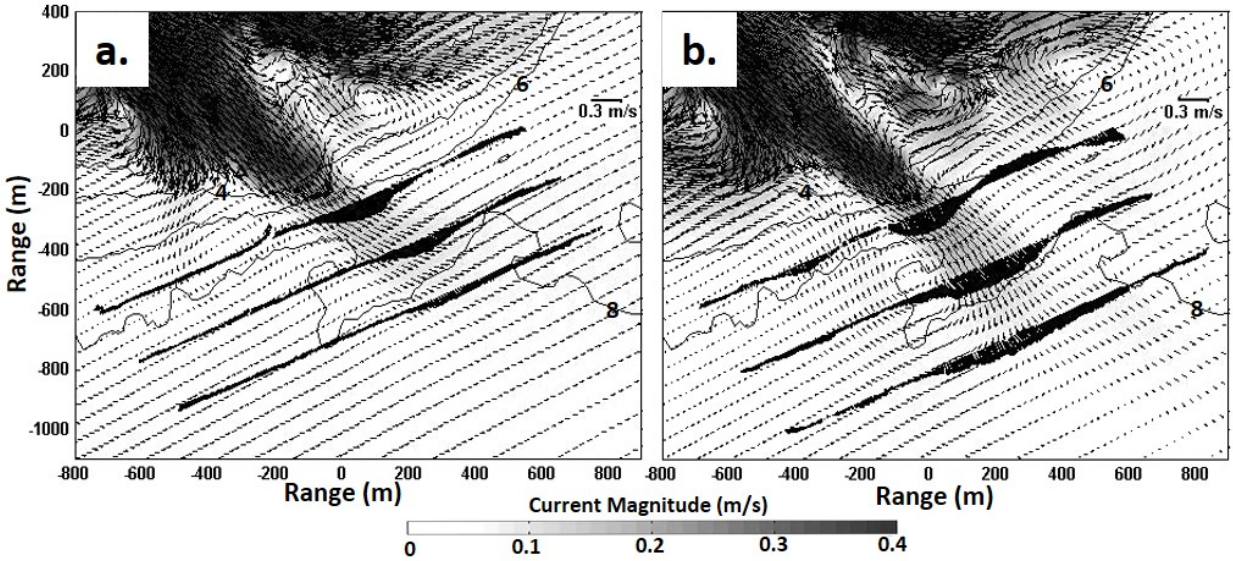

Figure 25. Depth-averaged velocity model output (black arrows, high resolution grid) overlaid with depth-averaged AUV velocity outputs for transects 1 through 3 (dark black arrow) for the (a) 5/17/2012 and (b) 5/19/2012 surveys. Bottom friction in random waves plus current flow is assumed for model runs. Numbers denote contours in meters.

The survey's results suggest that ambient ocean conditions (i.e. localized stratification, wind, and current) strongly influence the near-field and far-field characteristics of the discharged plume as it advects offshore. The mobility of the AUV coupled with modern observational instrumentation

enabled detailed characterization and analysis of the plume and its mixing at a resolution not possible by conventional mapping techniques. The methods utilized to observe the dynamic variability of the transitional region provide benchmark datasets for testing within coastal circulation models

IMPACT/APPLICATIONS

X-Band Radar

A data set of this size and resolution is a valuable asset for riverine science. We have the capability to track and measure relative water depth and shoaling activity through simple image averaging. This alone shows that X-Band radar can be used as a real time, remote sensing, river inlet hazard avoidance tool for mariners when visibility is limited. Additionaly, bottom morphology can be tracked by time series of backscatter averages over long periods of time. 3D spectral inversions can be used to remotely sense the change in impending waves, and therfore imply current and bathymetry measurements. Phase resolved wave inversions can accurately show wave refraction, breaking, and shoaling activity. Through a very narrow band frequency inversion, single wave trains can be analyzed through ray tracing for celerity to infer current and depth as well. Research is ongoing and methods are being improved and refined. We are looking forward to applying this research to the Mouth of the Columbia River.

REMUS AUV Surveys

AUV observations of the receiving waters of the New River Inlet yielded high resolution datasets of the dynamic mixing region where momemtum forces from the river discharge jet interact with the ambient ocean waters. There is potential to yield more synoptic datasets by improving velocity observations while the vehicle is undulating. Accurate velocity observations while the vehicle is sampling the water column would eliminate the need for repeat surveys at a constant depth, thus reducing mission time by approximately 50%. We have also illustrated the benefits of high resolution in-situ observations in the calibration of hydrodynamic coastal models. This effort was a collaboration with the UDEL (Hsu) team.

Minature Wave Buoys

The ability of wave buoys to measure wave properties in the surf zone is a novel advancement and will has a potential for supplementing wave models. The current wave models lack validation for areas of shoaling wave transformation such as the above directional spreading and significant wave height. The comparisons to X-Band backscatter are also an important new result in a shoaling environment. In both deep and shallow water, the mechanism for X-Band backscatter is similar and has been validated (HiRes project 2010). However, the good agreement between buoy significant wave height and X-Band return shows that X-Band radar can also be used to measure shoaling and breaking waves.

Wind Measurement Buoys

The effect of the steepening waves on the local coefficient of friction is a topic of continuing research. The observations made here are enough to suggest that an onshore wind will decelerate drastically as it encounters shoaling and steepening waves. The observation of the magnitude of this effect is a source of validation for a wind-wave coupled model.

RELATED PROJECTS

In-situ and Land-Based Remote Sensing of River Inlets and Their Interaction with Coastal Waters: Mouth of Columbia River.

REFERENCES

Ahmed, A.S.M., Takewaka, S., "PIV Analysis of Filtered Radar Images to Derive Nearshore Wave Properties and Bathymetry at Hasaki, Japan", Coastal Dynamics, 2005

Bell, P.S., "Shallow water bathymetry derived from an analysis of X-band marine radar images of waves", ELSEVIER Coastal Engineering, Vol. 37, 1999

Booij, N., Ris R.C., and Holthuijsen, L.H., "A third-generation wave model for coastal regions," *J. Geophys. Res.*, 104 (C4), 7649-7666, 1999.

Chen, J.-L, Shi, F., Hsu, T.-J. and Kirby, J. T., "NEARCOM-TVD - A quasi-3D nearshore circulation and sediment transport model," *Coastal Eng*, 91, 200-212, 2014.

Dugan, et. al., "Airborne Optical System for Remote Sensing of Ocean Waves", Journal of Atmospheric and Oceanographic Technology, Vol. 18, July 2001

Dugan, J.P., Piotrowski, C.C., Williams, J.Z., "Water depthe and surface current retrievals from airborne optical measurements of surface gravity wave dispersion", Journal of Geophysical Research, Vol. 106, No. C8, August 15, 2001

Dugan, J.P., Piotrowski, C.C, "Surface current measurements using airborne visible image time series", ELSEVIER Remote Sensing of the Environment, Vol. 84, 2003

Keulegan, G.H., "Tidal Flow in Entrances: Water Level Fluctuations of Basins in Communication with the Seas," *Committee on Tidal Hydraulics Technical Bulletin No.14*, U.S. Army Engineers Waterways Experiment Station, Vicksburg, MS., 1967.

Padilla-Hernández, R., and J. Monbaliu, "Energy balance of wind waves as a function of the bottom friction formulation." *Coastal Eng.*, 43, 131–148, 2001.

Plant, N.G., Holland, K.T., Haller, M.C., "Ocean Wavenumber Estimation from Wave-Resolving Time Series Imaging", IEEE Transactions on Geoscience and Remote Sensing, Vol. 46, No. 9, September 2008

Piotrowski, C.C., Dugan, P.J., "Accuracy of Bathymetry and Current Retrievals From Airborne Optical Time-Series Imaging of Shoaling Waves", IEEE Transactions on Geoscience and Remote Sensing, Vol. 40, No. 12, December 2002

Shi, F., Svendsen, I.A., Kirby, J.T., and Smith, J. M., "A curvilinear version of a Quasi-3D nearshore circulation model," *Coastal Eng.,* 49 (1-2), 99-124. 2003.

Soulsby, R.L., *Dynamics of marine sands*, Thomas Telford, London, 1997.

Svendsen, I.A., "Mass flux and undertow in a surf zone," *Coastal Eng*., 8, 347–365, 1984.